The Astronomical Journal, 141:139 (14pp), 2011 April doi:10.1088/0004-6256/141/4/139

CSO BOLOCAM 1.1 mm CONTINUUM MAPPING OF THE BRAID NEBULA STAR FORMATION REGION IN CYGNUS OB7

Colin Aspin[1], Tracy L. Beck[2], Chris J. Davis[3], Dirk Froebrich[4], Tigran Khanzadyan[5],
Tigran Yu. Magakian[6], Gerald H. Moriarty-Schieven[7], Tigran A. Movsessian[6], Sharon Mitchison[4],
Elena G. Nikogossian[6], Tae-Soo Pyo[8], and Michael D. Smith[4]
[1] Institute for Astronomy, University of Hawai'i, 640 N. A'ohoku Place, Hilo, HI 96720, USA; caa@ifa.hawaii.edu
[2] Space Telescope Science Institute, 3700 San Martin Drive, Baltimore, MD 21218, USA; tbeck@stsci.edu
[3] Joint Astronomy Centre, 660 N. A'ohoku Place, University Park, Hilo, HI 96720, USA; c.davis@jach.hawaii.edu
[4] Centre for Astrophysics & Planetary Science, School of Physical Sciences, The University of Kent, Canterbury CT2 7NR, UK;
smm23@kent.ac.uk, m.d.smith@kent.ac.uk
[5] Max-Planck Institut für Radioastronomie, Auf dem Hügel 69, Bonn, Germany; tkhanzadyan@mpifr-bonn.mpg.de
[6] V. A. Ambartsumyan Byurakan Astrophysical Observatory, Armenia; tigmag@sci.am, tigmov@bao.sci.am, elena@bao.sci.am
[7] NRC Herzberg Institute of Astrophysics, 5071 West Saanich Road Victoria, British Columbia, V9E 2E7, Canada; gerald.schieven@nrc-cnrc.gc.ca
[8] Subaru Telescope, National Astronomical Observatory of Japan, 650 N. A'ohoku Place, Hilo, HI 96720, USA; pyo@subaru.naoj.org

Received 2010 June 24; accepted 2011 January 27; published 2011 March 11

ABSTRACT

We present a 1.1 mm map of the Braid Nebula star formation region in Cygnus OB7 taken using Bolocam on the Caltech Submillimeter Observatory. Within the 1 deg^2 covered by the map, we have detected 55 cold dust clumps all of which are new detections. A number of these clumps are coincident with *IRAS* point sources although the majority are not. Some of the previously studied optical/near-IR sources are detected at 1.1 mm. We estimate total dust/gas masses for the 55 clumps together with peak visual extinctions. We conclude that over the whole region, approximately 20% of the clumps are associated with *IRAS* sources suggesting that these are protostellar objects. The remaining 80% are classed as starless clumps. In addition, both FU Orionis (FUor) like objects in the field, the Braid Star and HH 381 IRS, are associated with strong millimeter emission. This implies that FUor eruptions can occur at very early stages of pre-main-sequence life. Finally, we determine that the cumulative clump mass function for the region is very similar to that found in both the Perseus and ρ Ophiuchus star-forming regions.

Key words: ISM: clouds – ISM: jets and outflows – stars: formation

1. INTRODUCTION

A comprehensive review of the current state of star formation in the Cygnus molecular cloud complex was recently presented by Reipurth & Schneider (2008). One of the least studied of the nine OB associations in this region is Cygnus OB7 which is located at a distance of around 800 pc (Hiltner 1956; Schmidt 1958; de Zeeuw et al. 1999). The Cyg OB7 region contains several dark clouds which are collectively referred to as Kh 141 (Khavtassi 1960) and individually identified with Lynds catalog numbers (Lynds 1962). The dark cloud of interest here is LDN 1003 and was first investigated in the optical by Cohen (1980) who, while cataloging red nebulous objects, found it to contain a diffuse nebula which he designated RNO 127. Some time later, it was determined that RNO 127 was a bright Herbig–Haro (HH) object (HH 448; Melikian & Karapetian 2001, 2003). Both Devine et al. (1997) and Movsessian et al. (2003, henceforth M03) studied this region further and presented optical and near-IR (NIR) observations. Both groups found a number of new HH objects indicating the presence of a population of young star. With the presence of numerous *IRAS* sources, LDN 1003 was therefore confirmed as a site of significant star formation activity.

Of particular interest was the discovery of Movsessian et al. (2006, henceforth M06) who showed that an FU Orionis (FUor) eruptive variable (Ambartsumian 1971; Herbig 1989) was present in LDN 1003 and although not optically visible, it had brightened significantly in the NIR between the epoch of the Two Micron All Sky Survey (2MASS) image (taken in 1999) and those taken by Movsessian et al. (in 2001). In addition to the appearance of a bright, compact NIR source, they found that the associated NIR reflection nebula had also brightened. Further study revealed that the nebulosity appeared to form a double spiral or "braid" which seemed to have formed within the walls of two outflow cavities, one formed by high-velocity ejecta and the other by low-velocity outflow. The new FUor-like object was thus named "the Braid Star," although a General Catalog of Variable Stars (GCVS) identification is pending (to be included in GCVS Newsletter 80; N. Samus 2009, private communication).

Interestingly, some 30′ to the west of the Braid Star lies HH 381, a complex of shock-excited emission knots associated with a bright NIR point-like source, HH 381 IRS. In the optical and NIR HH 381 IRS was seen to possess a bipolar reflection nebula. What makes HH 381 IRS interesting is that when it was observed spectroscopically (Reipurth & Aspin 1997) it was discovered that it also exhibited many of the defining characteristics of an FUor. Further spectroscopic observations supported this interpretation (Greene et al. 2008) and a subsequent comparison of archival data (DSS-1 from 1953 and DSS-2 from 1990) with more recent CCD images demonstrated that as with the Braid Star, HH 381 IRS had brightened considerably over the last few decades (T. Yu. Magakian 2010, private communication). The presence of two FUors in LDN 1003 led us to believe that this region was worthy of a more intensive study.

Subsequently, a large-scale campaign focused on LDN 1003 was initiated. This covered a wide wavelength range (i.e., X-ray to millimeter) using a variety of observational techniques (i.e., imaging, spectroscopy, and polarimetry), with the aim of investigating the extent and characteristics of the young stellar population. The region of interest to us is a 1 deg^2 area centered on the FUor-like object, the Braid Star. This area also included the second FUor-like object present, HH 381 IRS.

Other papers in this series present studies of (1) optical and NIR broadband photometry of the stellar content of the region (S. Mitchison et al. 2011, in preparation), (2) optical and NIR shock-excited line emission present (Magakian et al. 2010, henceforth M10; T. Khanzadyan et al. 2011, in preparation), (3) the NIR spectroscopic characteristics of selected young stars (Aspin et al. 2009, henceforth A09), (4) the velocity structure of the submillimeter CO and HCN line emission (G. M. Moriarty-Schieven et al. 2011, in preparation; C. Aspin et al. 2011, in preparation), and (5) the newly discovered compact NIR [Fe II] emission jet from HH 381 IRS (T.-S. Pyo et al. 2011, in preparation). In this paper, the millimeter wavelength continuum emission from cold dust is studied using a 1.1 mm map of the region. With these data the population of compact dust clumps and their relationship to known optical and NIR sources are studied. Section 2 presents details of the observations and data reduction while Section 3 contains a description of the cold dust content of the region and identifies the compact clumps present. Section 4 compares the clump structure found with the location of known *IRAS* sources, young optical and NIR stars, and shock-excited nebulous objects. Section 5 attempts to relate the observations presented below to similar data on other star-forming regions. Lastly, Section 5 summarizes our discussions and presents our main conclusions.

2. OBSERVATIONS AND DATA REDUCTION

The data presented below were acquired on the Caltech Submillimeter Observatory (CSO), located on Mauna Kea, H I on UT 2009 June 30 and July 1. The facility millimeter bolometer array, Bolocam (Glenn et al. 1998), was used for the observations. It consists of a 144 element array of bolometers mounted at the Cassegrain focus of the 10.4 m CSO mirror. The field of view of the array is $7\farcm5 \times 7\farcm5$ and individual detectors have a near-Gaussian beam of $31''$ FWHM and a spacing of $38''$. The filter used was centered at 271.1 GHz (1.1 mm) and had a bandwidth of 46 GHz ($\Delta\nu/\nu = 0.17$). Our mapping strategy was similar to that adopted in obtaining the 170 deg^2 Galactic Plane Survey (GPS; Glenn et al. 2009). Briefly, the array bolometer was raster scanned across the region of interest by moving the CSO primary mirror which modulated the astronomical signal at a rate faster than changes in atmospheric opacity. In the case of the GPS, the raster scanning took place in galactic coordinates (l,b). For our observations, the 1 deg^2 field was covered using alternating raster scans in right ascension (R.A.) and declination (decl.). Each scan of the area of interest took approximately 20 minutes. The final map, created with $10''$ pixels, is therefore a combination of 30 raster scans (15 scans in each of R.A. and decl.). Flux calibration was achieved by twice nightly observations of both Neptune and Uranus. Pointing corrections were calculated approximately every 2 hrs using bright quasars. We note that the estimated uncertainty in position in the final map is of the order of $7''$. The standard IDL-based Bolocam reduction pipeline (Laurent et al. 2005) was used to create the final source map which has a rms noise of $\sigma \sim 17$ mJy beam^{-1}. For a more complete discussion of the data reduction techniques, the reader is referred to Enoch et al. (2006). The final 1.1 mm image was kindly analyzed by E. Rosolowsky using the custom source detection algorithm (*Bolocat*) developed specifically for the GPS (Rosolowsky et al. 2010). This analysis produced a catalog of discrete cold dust emission clumps including peak and integrated 1.1 mm fluxes, and information on the source morphology. A Monte Carlo simulation of clump recovery by Rosolowsky et al. (2010) found that the GPS was complete at the >99% level for a flux of 5σ sky rms (∼60% completeness at the 3σ level). This suggests that the completeness limit of our map is sources with integrated fluxes of 85 mJy beam^{-1}. Using Equation (3) of Enoch et al. (2006), this 5σ completeness limit corresponds to a clump mass limit of 2 and 0.7 $M_\odot$ for dust temperatures, T_D, of 10 and 20 K, respectively. The determination of an accurate T_D requires multiple wavelength observations (e.g., at 0.45, 0.85, and 1.1 mm) which are unavailable at this time. Since the T_D of the dust clumps is therefore unknown, our discussions below will consider values derived for both $T_D =$ 10 K and 20 K.

3. RESULTS

3.1. Definitions

Below we follow Di Francesco et al. (2007) by defining “protostellar” objects as 1.1 mm clumps with an associated *IRAS* source, and “starless” clumps as those without an *IRAS* detection. Protostellar clumps/cores possess embryonic stars still deeply embedded in molecular cloud and circumstellar gas and dust. Although these “Class 0” sources (Andre et al. 1993) emit at optical and NIR wavelengths, their flux is only observed via absorption and re-radiation at much longer wavelengths. Starless clumps have no internal luminosity sources and are therefore cold with dust temperatures of 10–20 K. A subset of starless clumps are the “prestellar” cores and the distinction is whether the clump is gravitationally bound and therefore has a mass that exceeds the Jeans mass (Ward-Thompson et al. 2007). Distinguishing between starless and prestellar clumps is not a simple matter and herein we will refer to all clumps with no *IRAS* association as starless clumps. We note that the *IRAS* 10σ detection limits of 0.7, 0.65, 0.85, and 3.0 Janskys at 12, 25, 60, and 100 μm, respectively, correspond to luminosity detection lower limits of 3.5, 1.6, 0.8, and 1.8 $L_\odot$ at a distance of 800 pc. With the above definitions in mind, therefore, we anticipate that we will detect both starless clumps and protostellar cores within our 1.1 mm map.

3.2. The 1.1 mm Continuum Map

Figure 1 shows the POSS-II digital sky survey red image of the region mapped at 1.1 mm. As can be seen, an extensive dark cloud complex is present which exhibits considerable compact and filamentary structure. In addition to the dark clouds, an extensive background stellar component is also present due to the galactic longitude of the field ($l \sim 91\fdg8$, $b \sim 4\fdg2$). Overlaid on the POSS-II image are contours of visual extinction (A_V) derived using NIR photometric data (UKIRT/WFCAM) in the manner described in Rowles & Froebrich (2009). The contours are for A_V values from 2 to 8 mag.

In Figure 2, we present our 1.1 mm map of this region. Numerous cold dust clumps of varying morphology are seen extending from the eastern to western edge of the map. Table 1 presents the list of clumps detected together with a designation (consistent with those given in the GPS), coordinates (equatorial and galactic), and integrated fluxes (in mJy). Also shown are any associations of clumps with previously detected objects, i.e., *IRAS* sources and optical/NIR stars.[9] Of the 55 clumps detected, 11 are coincident with *IRAS* sources (i.e., 20%). We have given each detected clump a numerical identification number (1–55, also given in Table 1) and the location of each is shown in

---

[9] No *Spitzer* data of this region exist.

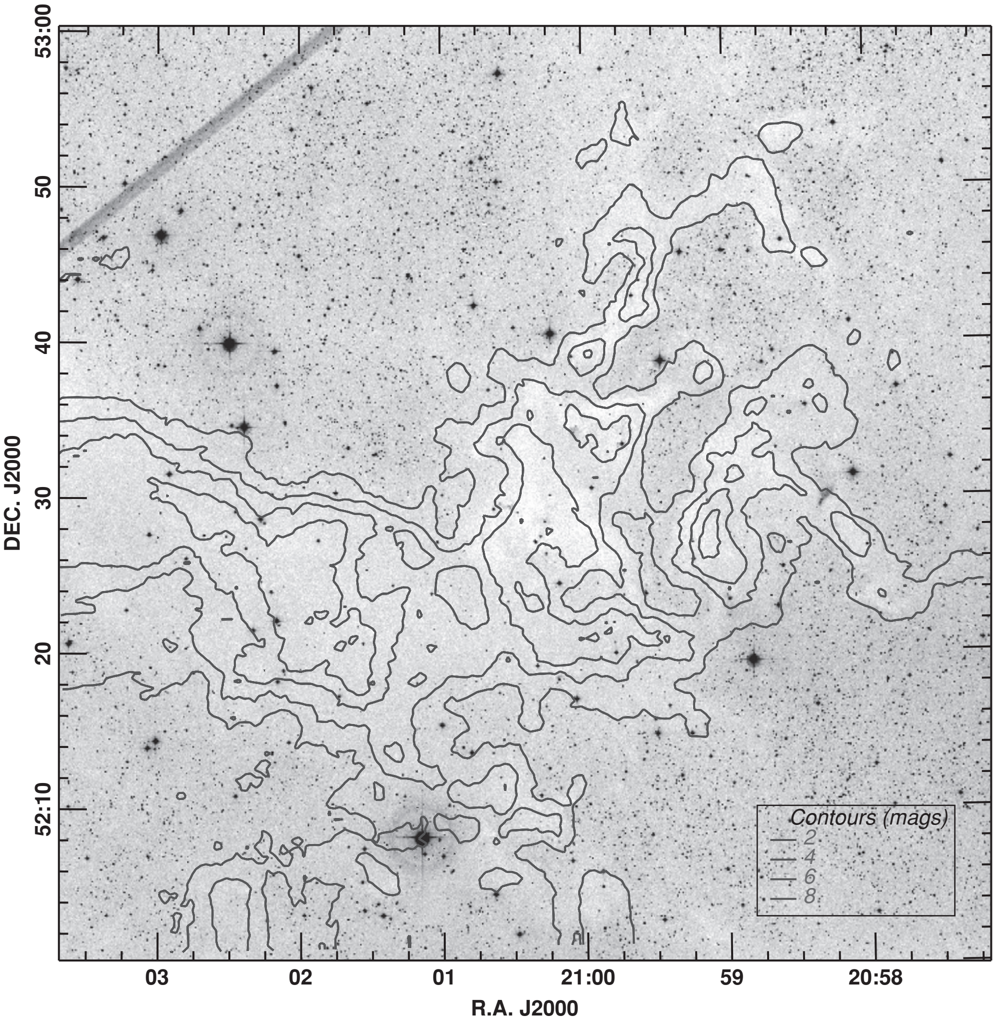

Figure 1. DSS-2 R-band image of the 1 $\deg^2$ region we have designated the Braid Nebula star formation region in Cygnus OB7 and which we have mapped at 1.1 mm using Bolocam. The image is centered on the newly discovered FUor-like object awaiting a GCVS designation and currently referred to as the Braid Star. The R-band image shows the extent of the dark cloud complex and is overlaid by contours of visual extinction derived from UKIRT WFCAM J,H,K photometry using the techniques of Rowles & Froebrich (2009).

Figure 3. As examples, we note that the Braid Star and HH 381 IRS are coincident with clumps #39 (G091.861+04.172) and #37 (G09.1638+04.398), respectively. Table 1 also shows the number of (10″) map pixels that each clump covers.

The correspondence between millimeter cold dust clumps and *IRAS* sources is demonstrated in Figure 4 where we overplot the *IRAS* source locations on the 1.1 mm map. Whereas the *IRAS* sources are relatively uniformly distributed over the whole 1 $\deg^2$ region, the millimeter clumps are clustered in the central band of the image following the location of the dark cloud complex (see the A_V contours in Figure 1). The aforementioned definitions (Section 3.1) suggest that the 11 *IRAS*/millimeter clump sources are all protostellar objects. Three other clumps are associated with optical/NIR sources, specifically Cyg 19, the Braid Star, and CN 6. As we shall see below, two of these three sources do exhibit weak emission in the far-IR (FIR).

3.3. Comparison of Optical/NIR Sources and Millimeter Clumps

A closer view of the central region of the 1.1 mm map is shown in Figure 5. The optical/NIR sources identified in M03, A09, and M10 are shown. A summary of the associations of these sources is given in Table 2. We find the following.

1. The Braid Star is closely related to clump #39 which has an integrated flux of ∼760 mJy. The star is classified as an FUor-like object based on both its NIR spectral structure and its recent optical/NIR brightening (M06). A09 commented on the peculiar fact that the Braid Star was not included in the *IRAS* Point-Source Catalog (*IRASPSC*). This is additionally surprising in light of the fact that it has now been found to be associated with significant cold dust emission. We have found that *HIRES* processed *IRAS* maps of the region showed weak FIR emission at the location of the Braid Star with fluxes of 17, 68, and 351 mJy at 12, 25, and 60 μm, respectively.[10]
2. HH 381 IRS is coincident with clump #37 which has an integrated flux of 495 mJy. This object is also classified as an FUor-like object based on the same criteria as for the Braid Star. The associated *IRAS* source, IRAS 20568 + 5217, has a small positional uncertainty ($\Delta a = 7''$, $\Delta b = 6''$) and lies directly on the NIR point source. HH 381 IRS

---

[10] The region was too confused at 100 μm to obtain a reliable flux estimate.

Table 1

Details of Millimeter Continuum Clumps Detected

Name of Clump	R.A. (J2000)	Decl. (J2000)	l^{a} (deg)	b^{b} (deg)	Flux[c] (mJy)	N_{pix}[d] #	ID[e]	Association[f]
G091.635+03.786	21:01:24.56	+52:05:03.9	91.6360	3.7860	149.8 ± 18	60	1	
G091.557+03.953	21:00:13.27	+52:08:16.1	91.5570	3.9530	130.1 ± 20	48	2	
G091.623+03.940	21:00:35.06	+52:10:58.7	91.6232	3.9405	269.7 ± 23	76	3	
G091.269+04.495	20:56:20.73	+52:16:16.0	91.2691	4.4948	176.9 ± 34	39	4	
G091.310+04.464	20:56:36.36	+52:16:45.4	91.3104	4.4643	261.7 ± 26	68	5	
G092.042+03.637	21:03:51.86	+52:17:24.2	92.0419	3.6374	133.1 ± 18	44	6	IRAS 21022 + 5205
G091.689+04.064	21:00:13.65	+52:18:41.3	91.6891	4.0639	128.3 ± 19	47	7	CYG19
G091.849+03.893	21:01:44.19	+52:18:43.3	91.8488	3.8932	156.0 ± 19	59	8	
G091.884+03.865	21:02:04.62	+52:19:22.0	91.8843	3.8651	210.0 ± 22	67	9	
G091.909+03.824	21:02:21.17	+52:18:50.1	91.9090	3.8240	252.0 ± 22	80	10	
G091.378+04.468	20:56:54.56	+52:20:11.6	91.3778	4.4675	216.7 ± 21	59	11	IRAS 20553 + 5208
G091.775+04.014	21:00:50.65	+52:20:14.7	91.7764	4.0144	186.7 ± 20	77	12	
G091.656+04.165	20:59:36.00	+52:21:00.3	91.6567	4.1646	156.7 ± 21	55	13	IRAS 20580 + 5208
G091.710+04.112	21:00:06.17	+52:21:28.7	91.7102	4.1116	535.7 ± 25	117	14	
G091.879+03.946	21:01:37.17	+52:22:10.2	91.8802	3.9461	470.9 ± 24	148	15	
G091.406+04.470	20:57:00.35	+52:21:30.3	91.4056	4.4695	194.6 ± 21	56	16	
G091.662+04.170	20:59:38.32	+52:21:53.9	91.6630	4.1700	60.46 ± 21	26	17	
G091.626+04.234	20:59:07.63	+52:22:21.7	91.6260	4.2337	548.6 ± 23	85	18	IRAS 20575 + 5210
G092.149+03.624	21:04:23.34	+52:21:57.6	92.1494	3.6240	133.3 ± 28	31	19	
G091.759+04.106	21:00:20.66	+52:23:24.6	91.7592	4.1062	238.3 ± 29	64	20	IRAS 20588 + 5211
G092.058+03.745	21:03:24.15	+52:22:41.1	92.0593	3.7445	230.5 ± 22	82	21	
G091.525+04.378	20:57:59.07	+52:23:31.0	91.5256	4.3785	180.1 ± 20	69	22	
G091.977+03.890	21:02:19.98	+52:24:40.3	91.9769	3.8901	84.15 ± 23	32	23	
G091.835+04.087	21:00:45.12	+52:26:03.4	91.8348	4.0871	124.5 ± 24	32	24	IRAS 20591 + 5214
G091.695+04.256	20:59:20.72	+52:26:55.4	91.6947	4.2564	102.7 ± 30	30	25	
G092.015+03.897	21:02:26.63	+52:26:17.1	92.0149	3.8973	307.5 ± 28	86	26	
G091.686+04.261	20:59:16.01	+52:26:10.1	91.6871	4.2609	223.7 ± 30	61	27	
G091.757+04.193	20:59:54.33	+52:26:47.0	91.7574	4.1930	157.6 ± 24	50	28	
G091.948+03.969	21:01:49.14	+52:26:35.9	91.9489	3.9689	217.9 ± 20	63	29	
G091.808+04.142	21:00:22.06	+52:26:59.3	91.8091	4.1421	117.7 ± 31	33	30	IRAS 20588 + 5215
G091.698+04.294	20:59:10.77	+52:27:31.4	91.6993	4.2935	264.3 ± 30	83	31	
G091.783+04.197	20:59:59.90	+52:28:03.5	91.7833	4.1971	88.34 ± 26	25	32	
G091.855+04.119	21:00:39.21	+52:28:28.1	91.8548	4.1192	856.1 ± 39	107	33	
G091.608+04.402	20:58:12.71	+52:27:59.7	91.6082	4.4023	173.7 ± 23	57	34	
G092.034+03.925	21:02:23.64	+52:28:30.5	92.0346	3.9254	930.6 ± 33	152	35	
G092.177+03.762	21:03:50.17	+52:28:40.8	92.1770	3.7618	375.1 ± 29	110	36	
G091.638+04.398	20:58:20.86	+52:29:17.2	91.6375	4.3983	484.9 ± 21	113	37	IRAS 20568 + 5217, HH381IRS
G091.813+04.201	21:00:05.70	+52:29:37.0	91.8132	4.2009	126.6 ± 23	35	38	
G091.861+04.172	21:00:27.17	+52:30:38.0	91.8605	4.1720	756.5 ± 40	129	39	Braid Star
G092.088+03.910	21:02:41.94	+52:30:20.8	92.0888	3.9098	401.5 ± 33	71	40	
G092.168+03.821	21:03:31.07	+52:30:32.4	92.1693	3.8214	214.0 ± 32	54	41	
G092.271+03.722	21:04:26.17	+52:31:16.8	92.2708	3.7217	178.4 ± 39	39	42	
G092.125+03.893	21:02:55.54	+52:31:16.7	92.1251	3.8935	712.7 ± 32	139	43	
G091.742+04.338	20:59:04.72	+52:31:38.2	91.7419	4.3378	1021.5 ± 37	155	44	
G091.828+04.273	20:59:45.93	+52:33:20.4	91.8282	4.2727	399.1 ± 23	103	45	
G092.197+03.853	21:03:27.74	+52:32:58.6	92.1972	3.8529	159.7 ± 32	37	46	
G091.741+04.377	20:58:54.61	+52:32:42.3	91.7407	4.3773	964.7 ± 35	119	47	IRAS 20573 + 5221, CN9
G092.269+03.787	21:04:06.58	+52:33:46.1	92.2695	3.7868	2230.4 ± 32	182	48	IRAS 21025 + 5221
G091.872+04.277	20:59:57.54	+52:35:09.8	91.8719	4.2775	110.6 ± 22	32	49	
G091.935+04.188	21:00:42.04	+52:34:32.2	91.9347	4.1884	61.66 ± 21	20	50	
G091.838+04.341	20:59:32.07	+52:36:01.5	91.8389	4.3409	359.8 ± 26	111	51	CN6
G092.250+03.869	21:03:38.21	+52:35:46.5	92.2497	3.8689	170.2 ± 29	38	52	
G092.263+03.882	21:03:37.74	+52:36:59.2	92.2644	3.8817	264.9 ± 26	57	53	
G091.926+04.343	20:59:52.77	+52:40:18.1	91.9259	4.3426	138.1 ± 23	37	54	IRAS 20583 + 5228, CN10
G091.957+04.543	20:58:59.98	+52:49:37.3	91.9578	4.5432	135.8 ± 18	51	55	

Notes.

[a] Galactic longitude.

[b] Galactic latitude.

[c] Uncertainties are calculated as in the Bolocam GPS, i.e., from the rms in the residual map created by subtracting the best-fit ellipsoid from the observed source (see J. E. Aguirre et al. 2011, in preparation for details).

[d] Number of map pixels in source.

[e] Identification number in Figure 3.

[f] Association with optical/NIR source.

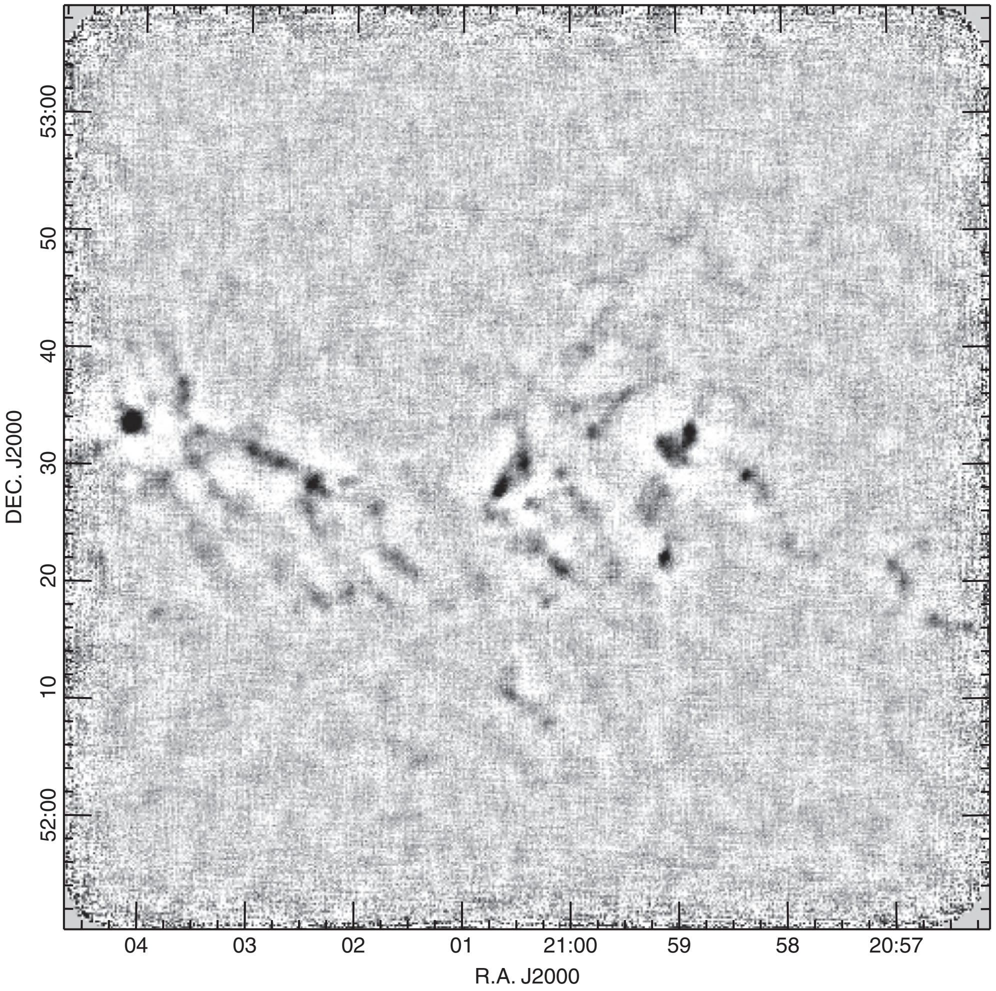

Figure 2. 1.1 mm Bolocam map of the region shown in Figure 1. This gray-scale representation shows the 55 detected cold dust clumps (black) on the featureless background (white). The clumps follow the dark cloud complex although they are considerably more structured than in the optical. The visual extinction contour (as shown in Figure 1) that encompasses all detected clumps is $A_V \sim 5$.

Table 2
Optical/NIR Source Associations

Object Name	2MASS ID	m_K (mag)	AKARI/IRC ID	AKARI/FIS ID	*IRAS* ID	MSX6C ID	1.1 mm ID
Braid Star	...	...	2100253+523017	2100249+523018	...	...	G091.813+04.201 (#39)
CN 1	21003517+5233244	12.5	2100352+523324	...	20590+5221	...	...
CN 1S	21003552+5233043	10.3	...	...	...	...	...
CN 2	21001656+5226230	10.7	...	...	...	...	...
CN 3N	21000376+5234290	10.0	2100038+523430	...	20585+5222	G091.8730+04.2583	...
CN 3S	21000508+5234049	10.8	...	...	...	...	...
CN4	20590895+5222392	11.3	...	...	...	...	...
CN5	20590419+5221448	12.2	...	...	...	...	...
CN 6	20594071+5234135	11.3	2059408+523414	...	...	G091.8313+04.2995	G091.838+04.341 (#51)
CN 6N	20594000+5234361	8.7	2059400+523436	...	...	...	...
CN 7	21001725+5228253	10.8	...	...	...	...	...
CN 8	21001903+5227281	9.8	2100191+522728	...	...	...	...
CN 9	20585089+5228254	14.8	...	...	...	...	...
CN 10	20595184+5240205	11.0	2059518+524020	...	20583+5228	G091.9269+04.3452	...
Cyg 19	21001159+5218172	10.0	...	...	...	...	G091.689+04.064 (#7)
HH381 IRS	20582109+5229277	8.3	2058211+522927	...	20568+5217	G091.6383+04.4007	G091.638+04.398 (#37)
HH627-STAR	20594446+5233213	10.4	...	...	...	...	...
IRAS 14[a]	21004237+5226007	14.1	2100423+522600	...	20591+5214	...	G091.835+04.087 (#24)
IRAS 15N[b]	21002140+5227094	9.4	2100215+522710	2100217+522712	20588+5215	...	G091.808+04.142 (#30)
IRAS 15S[b]	21002113+5227052	11.8	...	...	20588+5215	...	G091.808+04.142 (#30)

Notes.

[a] IRAS 14 is IRAS 20591+5214.

[b] IRAS 15N and 15S are the unresolved *IRAS* source 20588 + 5215.

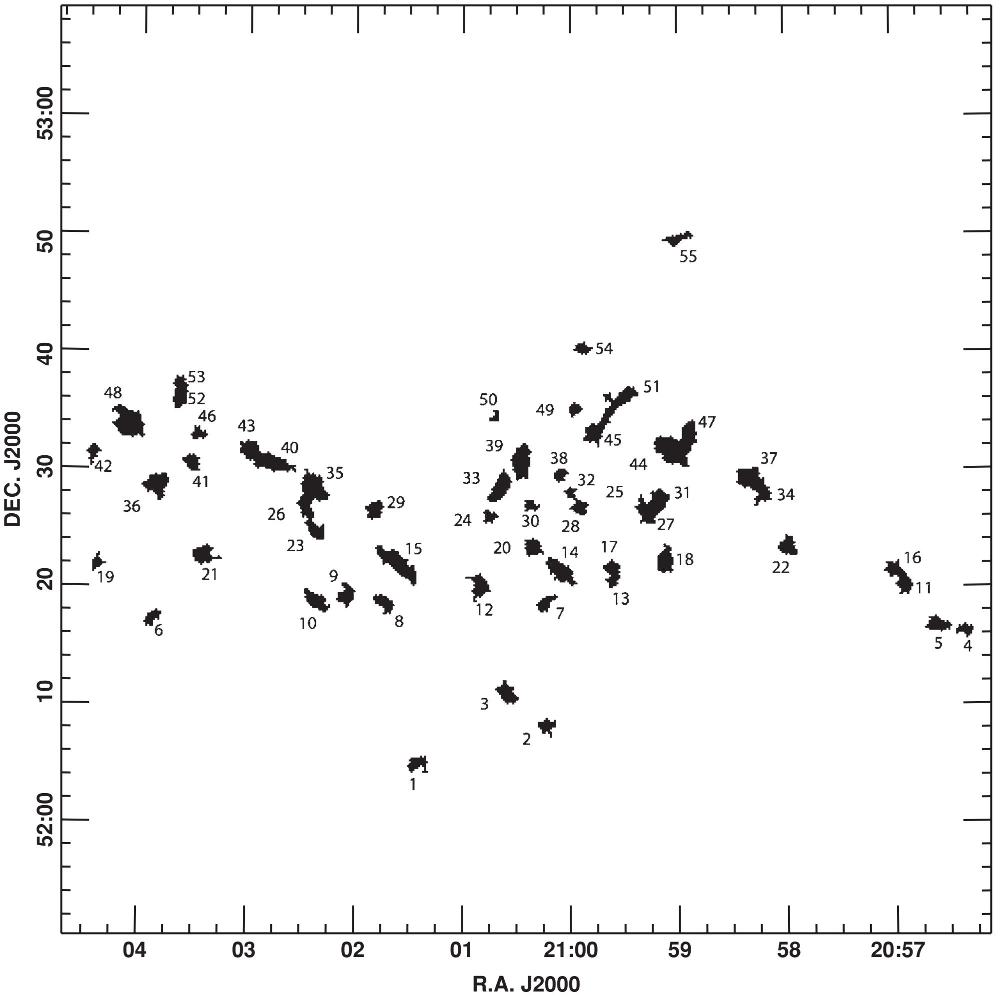

Figure 3. Object map of the compact cold dust clumps detected in the region. This map is the result of the structure detection analysis which finds discrete clumps (see Rosolowsky et al. 2010). The extent and shape of each detected clump is represented in black and each clump is numbered for identification purposes (see Table 3).

possesses a compact optical HH bipolar jet (M10) and extensive optical/NIR reflection nebulosity in a bipolar morphology.

3. CN 1 is a young star located ∼5′ northeast of the Braid Star. It possesses a monopolar cavity-like reflection lobe with a small-scale optical HH jet (HH 632, M10). It has a clear thermal NIR *K*-band excess (A09) and was found to be of approximately constant brightness at NIR wavelength between 2MASS observations (taken in 1999) and those of A09 (taken in 2006). The *IRAS* error ellipse includes CN 1, however, the *IRASPSC* only includes a good detection at 25 μm with flux, F_ν, ∼400 mJy. CN 1 does not appear to have a large amount of circumstellar dust since it is not obviously associated with a 1.1 mm dust clump.[11]
4. CN 1S is located some 30″ south of CN 1. It appears to be a moderately reddened early-type main-sequence dwarf (A09) and was not detected at 1.1 mm.
5. CN 2 is a fascinating young star and is a member of a small cluster located to the south of the Braid Star. This cluster includes CN 7, CN 8, and IRAS 15. M10 showed CN 2 to possess a non-collinear bipolar HH jet extending ∼±70″ (0.3 pc at 800 pc) to the north–northwest and southeast. Spectral template fitting by A09 classified it as an M2 ± 2 star with $A_V \sim 12$, and NIR veiling, r_K, of ∼0.4. At 1.1 mm, we find no compelling evidence of cold dust emission from CN 2 which was also not detected by *IRAS*.
6. CN 3 consists of two optically visible stars ∼30″ apart separated by a region of diffuse reflection nebulosity. The stars were designated CN 3N and 3S by A09. CN 3N has a 25 μm detection in the *IRASPSC* ($F_\nu \sim 500$ mJy) and the *IRAS* error ellipse encompasses CN 3N and excludes CN 3S. A09 estimated that CN 3N was a G8 dwarf with an $A_V \sim 20$, and $r_K \sim 0.2$. Neither CN 3N nor CN 3S were detected at 1.1 mm.
7. CN 4 is associated with a relatively strong 1.1 mm clump (#18) with a flux of 550 mJy. However, the 1.1 mm peak is slightly displaced from the *IRAS* coordinates. The *IRAS* error ellipse lies close to CN 4, although it is displaced in the direction of CN 5 which lies ∼90″ to the southwest. It is possible that this displacement is a result of contributions to the *IRAS* flux from both CN 4 and CN 5 (it was only detected at 60 μm with $F_\nu \sim 1.2$ Jy). M10 found both CN 4 and CN 5 to possess optical HH jets (HH 972 and 973, respectively). Both stars are therefore clearly young pre-main-sequence objects although only CN 4 seems to be associated with the 1.1 mm dust emission.
8. CN 6 is a compact nebula with an NIR excess and was classified as an embedded classical T Tauri star by A09

---

[11] As we noted above, our detection limit is $5\sigma \sim 2\ M_\odot$ for $T_D = 10$ K and $\sim 0.7\ M_\odot$ for $T_D = 10$ K.

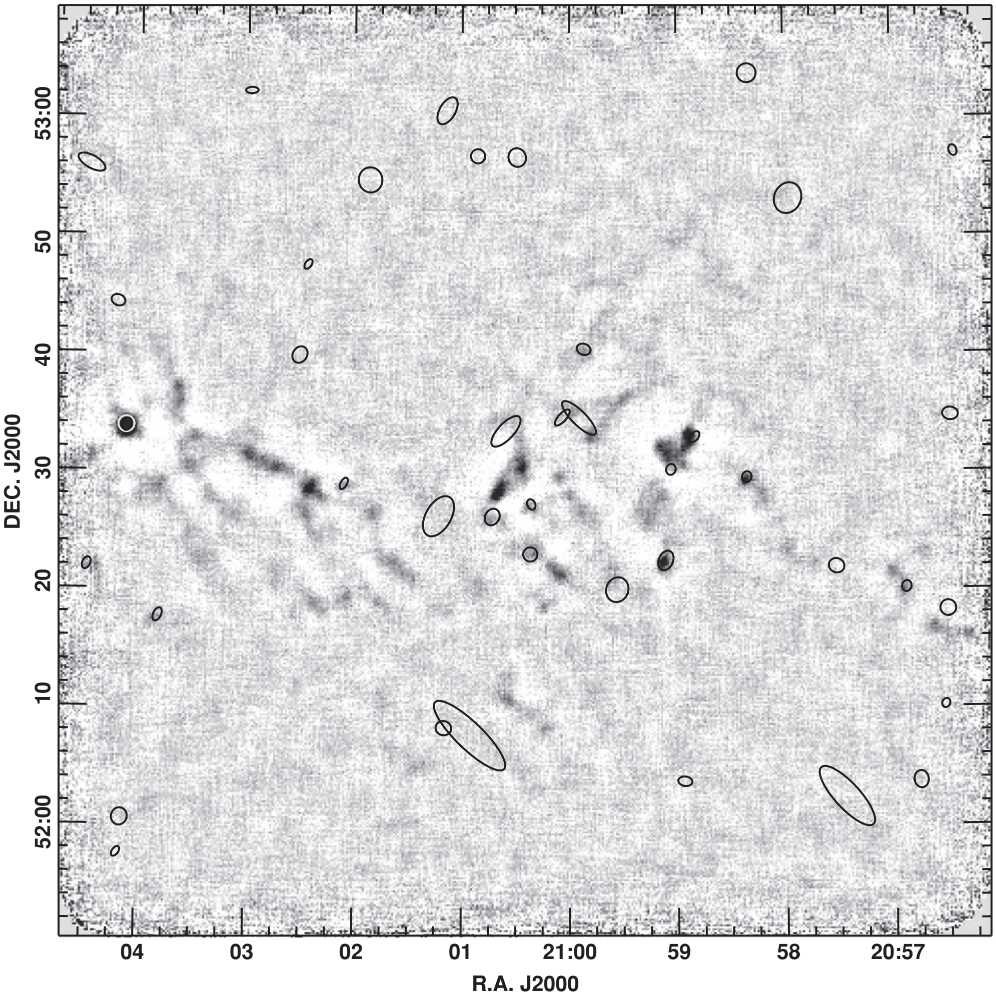

Figure 4. Gray-scale image of the region surveyed at 1.1 mm using Bolocam. The black (and one white) ellipses indicate the positions of the known *IRAS* sources in the region. The ellipses are displayed 4× the true size for clarity. Note the correspondence of many, but not all, millimeter clumps with *IRAS* sources.

with a spectral type between mid-G and mid-K. The 1.1 mm flux from the clump nearest CN 6 is ∼360 mJy although the morphology of the dust emission appears somewhat filamentary rather than clump-like. It seems likely that the clump is not physically associated with CN 6.

9. CN 7 is a member of the small cluster southwest of the Braid Star. In the optical, it possesses a small curving nebula and a compact point-like source (M10). Fitting the NIR spectrum of CN 7, A09 concluded it was most likely an M1 star with $A_V \sim 6$ and $r_K \sim 0.3$. Unusually, the young star associated with CN 7 showed no signs of active accretion exhibiting no Brγ emission. CN 7 is not included in the *IRASPSC*. CN 7 has no association with any HH objects and was not detected at 1.1 mm.
10. CN 8 is also a member of the small cluster southwest of the Braid Star. It has a monopolar cavity in the optical but no associated *IRAS* source (M10). In the NIR, it exhibits a small thermal excess and strong Brγ emission indicating it is surrounded by heated dust and is actively accreting. As with CN 7, CN 8 is not detected at 1.1 mm.
11. CN 9 is associated with an *IRAS* source (20573 + 5221) and an optical/NIR point source (M10). It also possesses a curving HH flow that extends to the southwest (HH 968) away from the optical/NIR star. No significant 1.1 mm emission is found in the immediate vicinity of CN 9.
12. CN 10 is seen at the northern edge of the image shown in Figure 5. M10 found that it possesses a point-like source which lies within the error ellipse of IRAS 20583 + 5228. Close by are the HH objects HH 975 which M10 suggested originate from the CN 10 star. This is supported by NIR shock-excited features (T. Khanzadyan et al. 2011, in preparation). At 1.1 mm, CN 10 is coincident with a faint dust clump (#54) with a flux of $F_\nu \sim 138$ mJy. Little else is known about CN 10 and its associated star.
13. Cyg 19 is an optical/NIR star with an associated curving nebulous feature. A09 concluded that Cyg 19 was a young K7 star possessing small visual extinction ($A_V \sim 5$) and NIR veiling ($r_K \sim 0.1$). It is located close to clump #7 in our 1.1 mm map, a weak feature with an integrated flux of ∼130 mJy. It was not detected by *IRAS*, although *HIRES*-processed *IRAS* images show a weak detection ($F_\nu(12\,\mu\mathrm{m}) \sim 15$ mJy, $F_\nu(25\,\mu\mathrm{m}) \sim 80$ mJy, $F_\nu(60\,\mu\mathrm{m}) \sim 338$ mJy, and $F_\nu(100\,\mu\mathrm{m}) \sim 3.4$ Jy).
14. IRAS 14 (20591+5214) was very weakly detected in the optical images of M10 and has been proposed as the originating source of HH 633 located some 50″ south. In the NIR, it is associated with a point source of $m_K \sim 14$. The *IRASPSC* only has a good detection of the source at 25 μm ($F_\nu(25\,\mu\mathrm{m}) \sim 420$ mJy) with upper limits in the other *IRAS* bands. The *IRAS HIRES* image gave flux

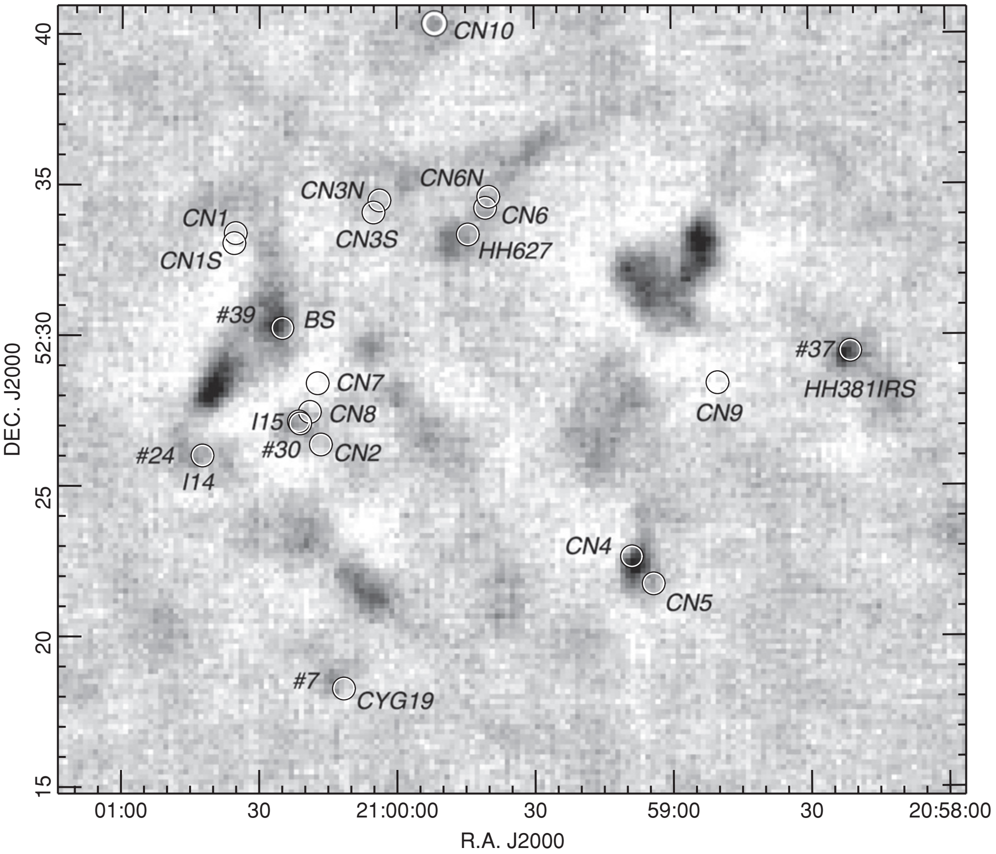

Figure 5. Gray-scale image of the region of the central region of the 1.1 mm Bolocam image. The black/white circles indicate the positions of the optical/NIR sources in the region, many observed spectroscopically in A09. The hashed numbers are the clump identifications from Figure 3.

values of $F_\nu(12\,\mu\mathrm{m}) \sim 13$ mJy, $F_\nu(25\,\mu\mathrm{m}) \sim 308$ mJy, $F_\nu(60\,\mu\mathrm{m}) \sim 890$ mJy, and $F_\nu(100\,\mu\mathrm{m}) \sim 9.6$ Jy reasonably consistent with the *IRASPSC* limits. A relatively weak 1.1 mm clump (#24) is found at the location of IRAS 14 and has an integrated flux of 125 mJy.

15. IRAS 15 (20588 + 5215) is bright in both optical and NIR bands. It is a close double star (IRAS 15N and 15S) with a separation of $\sim 5''$. IRAS 15N is significantly brighter in the NIR than IRAS 15S although in the optical both sources appear of similar brightness. A09 suggested that IRAS 15N is an actively accreting young star with strong Brγ and CO overtone bandhead emission. They concluded that IRAS 15S may be a foreground object (an early-K dwarf). The *IRASPSC* fluxes for the combined object are $F_\nu(12\,\mu\mathrm{m}) \sim 642$ mJy, $F_\nu(25\,\mu\mathrm{m}) \sim 3.0$ Jy, $F_\nu(60\,\mu\mathrm{m}) \sim 8.2$ Jy, and $F_\nu(100\,\mu\mathrm{m}) < 9.6$ Jy. IRAS 15 appears to be associated with a 1.1 mm clump (#33) with integrated flux of 118 mJy. Due to their close proximity, IRAS 15N and 15S are not resolved in our millimeter-continuum map.

Of the 20 sources, 19 are 2MASS sources, six are *IRAS* sources, four are included in the MSX6C catalog, 10 were detected by AKARI/IRC,[12] two were detected by AKARI/FIS,[13] and six have measurable 1.1 mm emission. Only three sources have both *IRAS* and millimeter associations (specifically, HH 381 IRS, IRAS 14, and IRAS 15). This number becomes five if we include the two sources with faint detections in the *HIRES* processed *IRAS* images (i.e., the Braid Star and Cyg 19).

3.4. HH Jets and Dust Clumps

In Figure 6, we show a narrowband Hα image of the central $60' \times 40'$ of the region surveyed at 1.1 mm. This Subaru/Suprime-cam image is taken from M10 who cataloged the optical shock-excited HH objects in this region. Overlaid on the Hα image are contours of 1.1 mm dust emission. We note that the millimeter clumps are well aligned with the dark cloud complexes seen at optical wavelengths. Almost all optically dark regions have associated millimeter clumps. In order to more clearly see the correspondence of optical and millimeter structures, we present below expanded views of several regions containing interesting optical/NIR features.

3.4.1. The Braid Star Region

In Figure 7, we have labeled the optical/NIR sources present, specifically CN 1, CN 2, CN 3, CN 7, CN 8, and IRAS 15N&S. The Braid Star is also indicated as is IRAS 14, both of which have no optical/NIR counterpart. Several interesting features are evident in this image.

1. The Braid Star lies very close to a peak of 1.1 mm dust emission (#39) and both the HH flow extending from it to the southwest (HH 629) and the optical reflection nebulosity are visible only from the edge of the cold dust clump.
2. A second strong millimeter clump is seen to the southeast of clump #39. This has the identification #33. On the edge of this emission peak is the group of HH objects previously designated RNO 127 (Cohen 1980) and more recently found to be HH objects (HH 448, M03). M10 found additional HH objects in this region, which they designated

---

[12] AKARI is the Japanese infrared space telescope (formerly ASTRO-F). IRC is the AKARI InfraRed Camera.

[13] FIS is the AKARI Far-Infrared Surveyor camera.

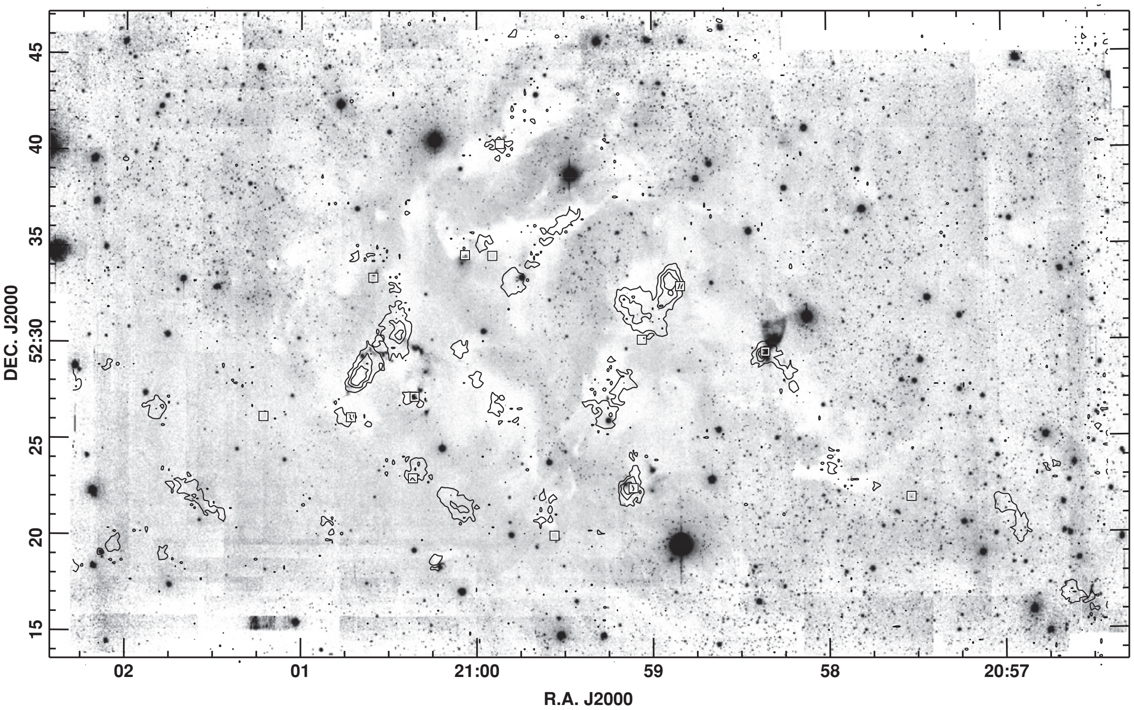

Figure 6. Subaru/Suprime-cam optical Hα image from Magakian et al. (2010), covering part of the region surveyed using Bolocam. Contours of the 1.1 mm flux are overlaid. The black/white squares indicate the *IRAS* sources in the region.

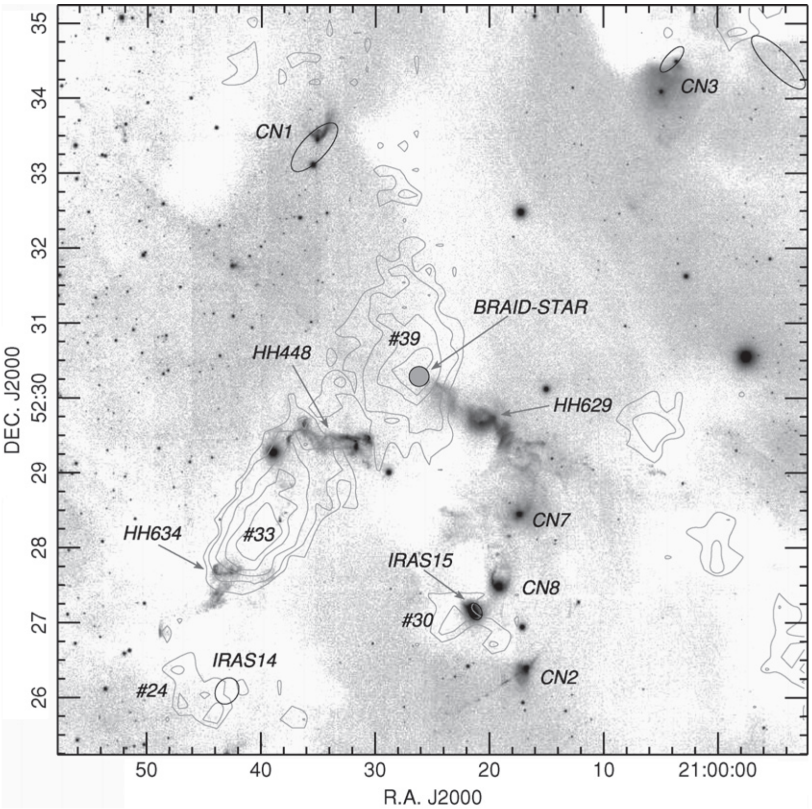

Figure 7. Region of the optical Hα image shown in Figure 6 covering the Braid Nebula, CN 1–3, CN 7–8, and IRAS 14 and 15. Contours of 1.1 mm dust emission are overlaid. The contour levels are 40, 60, 80, 100, and 140 mJy. The Braid Star is indicated by the gray circle. The *IRAS* sources in the region are shown as black error ellipses. The hashed numbers (e.g., #33) are the millimeter clump identification numbers from Table 1.

HH 634 (see their Figure 19). HH 448 and 634 are located at the northwest and southeast boundaries of millimeter clump #33, respectively, and the apparent direction of propagation of HH 634 appears to be from the center of it.

3. As we related above, the two *IRAS* sources IRAS 14 and 15N&S are associated with weak millimeter clumps (#24 and #30, respectively). IRAS 15N&S are optically visible while IRAS 14 is totally obscured. IRAS 14 can

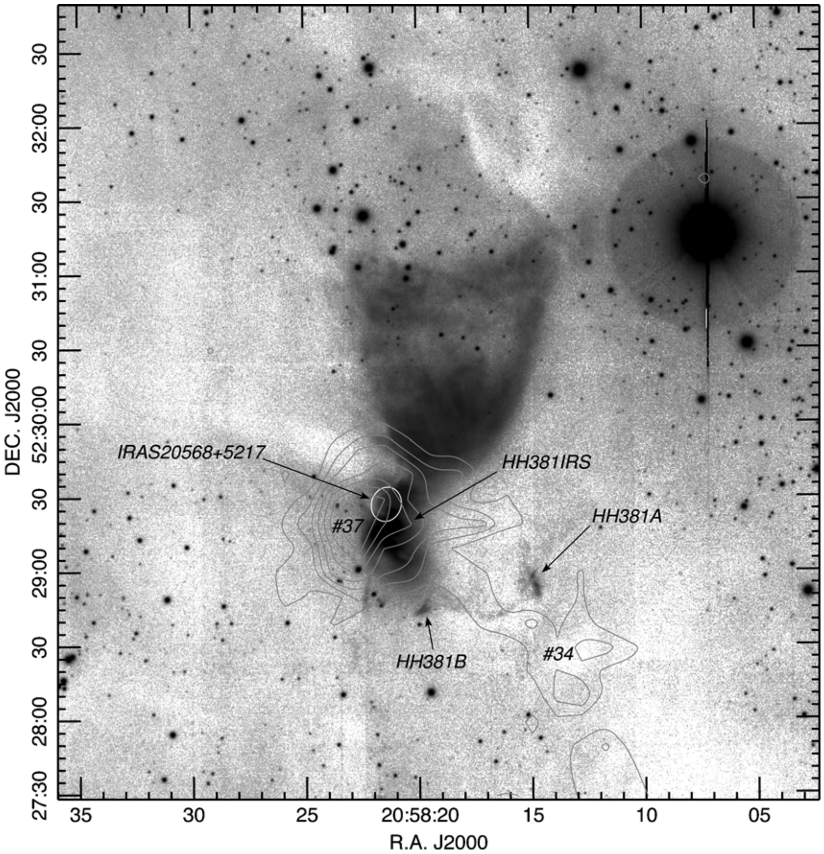

Figure 8. Region of the optical Hα image shown in Figure 6 covering HH 381 IRS. Contours of 1.1 mm dust emission are overlaid. The contour levels are 40, 60, 80, 100, 140, and 180 mJy. The *IRAS* source associated with HH 381 IRS is shown as a white error ellipse. The hashed numbers (e.g., #37) are the millimeter clump identification numbers from Table 1.

therefore be deemed a protostellar core while IRAS 15N&S are somewhat problematic since the association of *IRAS* source and millimeter clump implies a protostellar nature yet the visible nature of the source implies a more evolved young star. One explanation could be that we are viewing IRAS 15N&S from a preferential direction, i.e., along a cleared outflow axis rather than through a dense dust disks. Alternatively, the *IRAS* source and millimeter clump may be spatially separated along the line of sight with the two young optically visible stars and millimeter clump not being physically related. IRAS 15 would then be interpreted as a protostellar object while the two visible stars being foreground to it.

4. A number of weak millimeter clumps in Figure 7 have no associated optical nor NIR counterparts. None have associated *IRAS* sources and hence we can consider them to be starless clumps.

To summarize, therefore, this $10' \times 10'$ sub-region of the survey area contains at least three protostellar objects, six Class II sources (criteria for classification defined in A09), and eight starless clumps.

The ratio of the number of protostellar cores ($N_{\rm psc}$) to starless clumps ($N_{\rm slc}$) is potentially an important diagnostic of the core/star formation process. Lee & Myers (1999) investigated a large sample of optically selected dark clouds throughout the galactic plane for core structure and found an overall ratio $N_{\rm psc}/N_{\rm slc}$ of 0.31. Under simple assumptions, they related the above ratio to the lifetime of the protostellar (Class 0 + I) phase ($t_p = 1$–5×10^5 yr) with respect to the core formation timescale (t_c). They noted that ambipolar diffusion models predicted t_p/t_c values of between 0.007 and 0.14 which were considerably smaller than observed. This discrepancy they considered evidence for a predicted model core formation timescale that was too long compared to direct observations. For the Braid Star region, we find a ratio $N_{\rm psc}/N_{\rm slc} \sim 0.37$ (3/8, not including the two faint *IRAS* hire detections), but clearly there is a large uncertainty due to small number statistics. Davis et al. (2010) found a ratio of $\sim$0.5 for the Taurus star formation cloud L1495; however, such a cloud is perhaps not an appropriate comparison to the more distant Cyg OB7 complex. Lee & Myers (1999) concluded that a typical lifetime of a starless core may be around three times longer than the protostellar phase which is consistent with our above result.

3.4.2. The HH 381 IRS Region

Figure 8 shows a $5' \times 5'$ region of the Hα image centered on HH 381 IRS. Extending from this source to the north is a conical reflection nebula, most likely an outflow cavity illuminated by the central star or circumstellar region. A less extensive southern counterpart to this structure is present but is mostly obscured in the optical and seen best in the 2 μm image shown in A09 (Figure 2).

The central star, HH 381 IRS, is associated with a strong *IRAS* source and our 1.1 mm map shows it is also associated with a compact millimeter clump (#37) with an integrated flux of 485 mJy. Within the uncertainties in the millimeter map coordinate system (see above) and the *IRAS* error ellipse, the millimeter clump peak can be considered coincident with both *IRAS* source and HH 381 IRS itself.

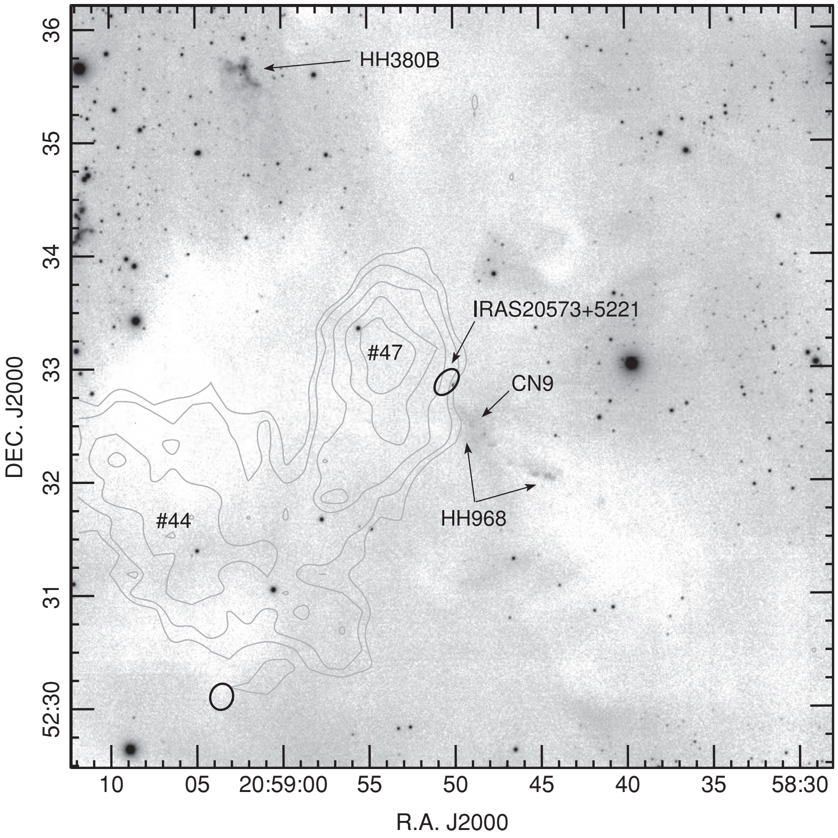

Figure 9. Region of the optical Hα image shown in Figure 6 covering CN 9. Contours of 1.1 mm dust emission are overlaid. The contour levels are 40, 60, 80, 100, and 140 mJy. The IRAS source nearest CN9 is shown as a black error ellipse. The hashed numbers (e.g., #47) are the millimeter clump identification numbers from Table 1.

Finally, we note that millimeter clump #37 appears to have a tail extending to the southwest toward clump #34 and which follows the optical dark cloud complex.

3.4.3. The CN 9 Region

Figure 9 shows the 6′ × 6′ region of the Hα image immediately surrounding the compact nebula designated CN 9 by M10. CN 9 is associated with the HH flow HH 968 and the *IRAS* source 20573 + 5221. A millimeter clump (#47) is present near the *IRAS* source and located along an axis defined by HH 968, CN 9, and the *IRAS* source. The millimeter clump peak is located ∼45″ from the center of the *IRAS* error ellipse; however, it appears that the young star that is driving the HH 968 flow is most likely located in clump #47.

3.4.4. The HH 627 Region

Figure 10 comprises a 2′ × 2′ sub-section of the Hα image centered on the bright star near HH 627. The image is overlaid with contours of 1.1 mm emission. The bright star was considered to be a foreground main-sequence object (A09) even though the morphology of the compact flow HH 627 appears to extend away from it. A millimeter clump (#45) lies close to the foreground star and HH 627 is located between the foreground object and the clump #45. The most likely scenario is that the young star driving the HH 627 flow is embedded in millimeter clump #45.

The compact nebula CN 6 is also seen in this region. This object lies close to a very weak millimeter clump that forms part of clump #51 in Figure 3. It is not clear whether CN 6 and this weak millimeter clump are related.

4. DISCUSSION

4.1. Properties of the Cold Dust Clumps

If we adopt values for dust temperature, T_D, dust opacity, $\kappa_{1.1\,\mathrm{mm}}$, column density to visual extinction conversion ratio, $N(\mathrm{H}_2)/A_V$, gas-to-dust ratio, and cloud distance, we can estimate the total mass of the clumps, together with the peak column density and visual extinction toward the observed flux peak. Cold dust clouds with no internal heating source should have typical temperatures of ∼10 K (Bergin & Tafalla 2007). This may increase in dust clumps to up to perhaps 20 K. For the determination of clump mass, H_2 column density, and A_V we adopt $T_D = 10$ K but note that for $T_D = 20$ K all three values will be 2.9× smaller (1.9× smaller for $T_D = 15$ K). Additionally, we assume $\kappa_{1.1\,\mathrm{mm}} = 0.0114\ \mathrm{cm}^2\ \mathrm{g}^{-1}$ (Enoch et al. 2006 extrapolated from tabulated data by Ossenkopf & Henning 1994 for dust grains with thin ice mantles coagulated for 10^5 yr at a gas density of $10^6\ \mathrm{cm}^{-3}$), $N(\mathrm{H}_2)/A_V) = 0.94 \times 10^{21}\ \mathrm{cm}^2\ \mathrm{mag}^{-1}$ (Frerking et al. 1982), a gas-to-dust ratio of 100:1, and a distance of 800 pc.

Following Enoch et al. (2006), we use Equation (1) to estimate clump masses:

$$M_{\mathrm{clump}} = d^2 S_\nu / B_\nu(T_D)\kappa_\nu, \tag{1}$$

where d is the source distance, S_ν is the total flux density of the source, $B_\nu(T_D)$ is the blackbody flux at temperature T_D, and κ_ν is the aforementioned dust opacity. Additionally, we calculate peak H_2 column densities, $N(\mathrm{H}_2)$, from the peak flux in each

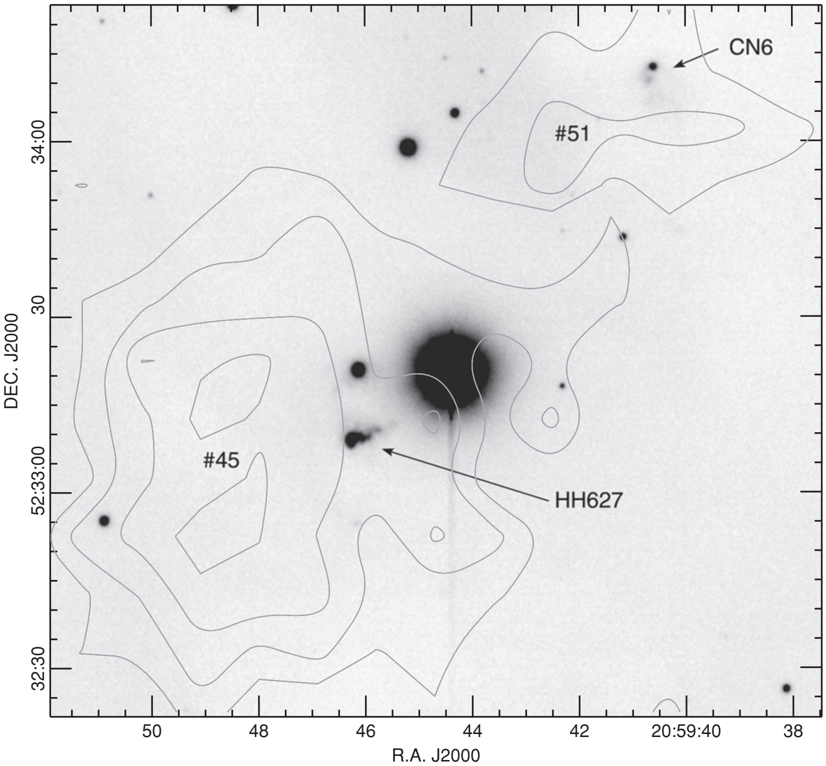

Figure 10. Region of the optical Hα image shown in Figure 6 covering HH 627. Contours of 1.1 mm dust emission are overlaid. The contour levels are 40, 60, 80, and 100 mJy. The hashed numbers (e.g., #45) are the millimeter clump identification numbers from Table 1.

clump using Equations (2):

$$N(\mathrm{H}_2) = S_\nu^{\mathrm{beam}}/\Omega_{\mathrm{beam}}\mu_{\mathrm{H}_2} m_H \kappa_\nu B_\nu(T_D), \qquad (2)$$

where S_ν^{beam} is the peak flux per beam in the clump, Ω_{beam} is the solid angle subtended by the Bolocam beam, μ_{H_2} is the mean molecular weight per H_2 molecule ($\mu_{\mathrm{H}_2} = 2.8$), and m_H is the mass of the hydrogen atom. We use the conversion factor related above to convert $\mathrm{N(H_2)}$ to A_V.

Table 3 presents the results of this analysis showing the observed values of integrated and peak flux together with derived values for M_{clump}, $N(\mathrm{H}_2)$, and A_V. The quoted errors on the integrated fluxes consider several sources of uncertainties and are produced by the *Bolocat* extraction process. The contributory sources of error, and their combination, are explained in detail in Rosolowsky et al. (2010). The uncertainties on the peak flux is the rms value in sky regions with no detected cold dust emission (i.e., 17 mJy beam^{-1}). For $T_D = 10$ K, M_{clump} values range from 1.5 $M_\odot$ (integrated flux of ~60 mJy) to 54 $M_\odot$ (integrated flux of ~2.23 Jy). A_V values range from 2 to 28 mag. The total mass of gas and dust in the region is ~439 $M_\odot$.

Although the usefulness of a clump mass function has been brought into question by the modeling of Reid et al. (2010),[14] we consider below such an analysis for completeness and for comparison to other similar surveys. Therefore, a plot of the cumulative clump mass function (CCMF) for these 55 clumps is shown in Figure 11. This plot is of similar form to that of Johnstone et al. (2000, see their Figure 7) who found the same number of clumps (55) at 850 μm in the ρ Ophiuchus star-forming cloud. We note that the CCMF of Johnstone et al. extends to much lower masses, specifically 0.02 $M_\odot$ for the value of T_D they used, i.e., $T_D = 20$ K (this becomes ~0.06 $M_\odot$ for $T_D = 10$ K) as opposed to 1.5 $M_\odot$ from our observations. This is the result of both the closer distance to ρ Oph (160 pc as opposed to 800 pc) and the fact that they observed at 850 μm and not 1.1 mm, hence providing improved sensitivity of a quoted 10 mJy beam^{-1} rms noise as opposed to our 17 mJy beam^{-1}. The mass spectrum in ρ Oph was found to be best represented by a split power law (each of the form $M^{-\alpha}$) with slopes of $\alpha = 0.5$ and 1.5 for low- and high-mass regions, respectively. The split in the power-law fit occurred at ~0.6 $M_\odot$. Johnstone et al. however noted that the low-mass end of the mass spectrum

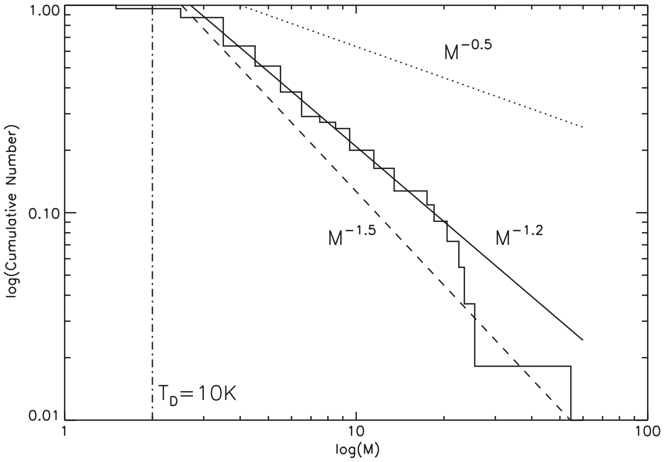

Figure 11. Cumulative mass function for the survey region. The Y-axis has been normalized to unity corresponding to all 55 cold dust clumps. The >99% completeness limit is shown by the vertical dot-dashed line at 2 $M_\odot$ (for $T_D = 10$ K). Mass functions of the form $M^{-\alpha}$ are shown and correspond to α values of 1.5 (dashed line), 0.5 (dotted line), and 1.2 (solid line) where $\alpha = 1.2 \pm 0.15$ is the best-fit value between 2 and 20 $M_\odot$.

---

[14] Reid et al. (2010) found that source blending, noise, and spatial filtering all conspired tended to produce a Salpeter-like log-normal power-law distribution.

Table 3
Properties of Millimeter Continuum Clumps

Name	ID[a] \#	Flux[b] (mJy)	Mass[c] $M_\odot$	Peak Flux[d] (mJy beam^{-1})	N(H_2)[e] (cm^{-2})	A_V[f] (mag)	a[g] (″)	b[h] (″)	P.A.[i] (deg)
G091.635+03.786	1	150 ± 18	3.7 ± 1.0	32 ± 17	2 ± 1e21	2 ± 1	45	20	113 ± 5
G091.557+03.953	2	130 ± 20	3.2 ± 1.0	38 ± 17	2 ± 1e21	3 ± 1	28	18	104 ± 5
G091.623+03.940	3	270 ± 23	6.6 ± 1.5	59 ± 17	4 ± 1e21	4 ± 1	37	20	47 ± 5
G091.269+04.495	4	177 ± 34	4.3 ± 1.6	59 ± 17	4 ± 1e21	4 ± 1	38	18	93 ± 5
G091.310+04.464	5	262 ± 26	6.4 ± 1.6	57 ± 17	4 ± 1e21	4 ± 1	33	23	67 ± 5
G092.042+03.637	6	133 ± 18	3.3 ± 1.0	41 ± 17	3 ± 1e21	3 ± 1	33	18	129 ± 5
G091.689+04.064	7	128 ± 19	3.1 ± 0.1	42 ± 17	3 ± 1e21	3 ± 1	26	18	151 ± 5
G091.849+03.893	8	156 ± 19	3.8 ± 1.1	39 ± 17	3 ± 1e21	3 ± 1	52	18	51 ± 5
G091.884+03.865	9	210 ± 22	5.1 ± 1.4	49 ± 17	3 ± 1e21	3 ± 1	31	21	150 ± 5
G091.909+03.824	10	252 ± 22	6.2 ± 1.5	50 ± 17	3 ± 1e21	3 ± 1	51	20	49 ± 5
G091.378+04.468	11	216 ± 21	5.3 ± 1.2	55 ± 17	4 ± 1e21	4 ± 1	34	18	2 ± 5
G091.775+04.014	12	187 ± 20	4.6 ± 1.3	36 ± 17	2 ± 1e21	3 ± 1	40	24	8 ± 5
G091.656+04.165	13	157 ± 21	3.8 ± 1.2	39 ± 17	3 ± 1e21	3 ± 1	52	20	155 ± 5
G091.710+04.112	14	536 ± 25	13.0 ± 2.1	90 ± 17	6 ± 1e21	6 ± 1	47	22	50 ± 5
G091.879+03.946	15	471 ± 24	11.5 ± 2.3	53 ± 17	3 ± 1e21	4 ± 1	77	24	51 ± 5
G091.406+04.470	16	195 ± 21	4.8 ± 1.2	58 ± 17	4 ± 1e21	4 ± 1	27	20	46 ± 5
G091.662+04.170	17	60 ± 21	1.5 ± 0.8	35 ± 17	2 ± 1e21	2 ± 1	22	18	. . .
G091.626+04.234	18	549 ± 23	13.4 ± 1.8	140 ± 17	9 ± 1e21	10 ± 1	29	19	159 ± 5
G092.149+03.624	19	133 ± 28	3.3 ± 1.2	47 ± 17	3 ± 1e21	3 ± 1	33	18	148 ± 5
G091.759+04.106	20	238 ± 29	5.8 ± 1.8	54 ± 17	4 ± 1e21	4 ± 1	31	28	31 ± 5
G092.058+03.745	21	230 ± 22	5.6 ± 1.5	41 ± 17	3 ± 1e21	3 ± 1	37	30	82 ± 5
G091.525+04.378	22	180 ± 20	4.4 ± 1.2	37 ± 17	2 ± 1e21	3 ± 1	36	24	6 ± 5
G091.977+03.890	23	84 ± 23	2.1 ± 1.0	31 ± 17	2 ± 1e21	2 ± 1	40	23	49 ± 5
G091.835+04.087	24	124 ± 24	3.0 ± 1.0	48 ± 17	3 ± 1e21	3 ± 1	24	18	. . .
G091.695+04.256	25	103 ± 30	2.5 ± 1.2	47 ± 17	3 ± 1e21	3 ± 1	57	18	5 ± 5
G092.015+03.897	26	307 ± 28	7.5 ± 1.9	58 ± 17	4 ± 1e21	4 ± 1	87	18	16 ± 5
G091.686+04.261	27	224 ± 30	5.5 ± 1.7	52 ± 17	3 ± 1e21	4 ± 1	37	22	171 ± 5
G091.757+04.193	28	158 ± 24	3.9 ± 1.3	45 ± 17	3 ± 1e21	3 ± 1	32	21	13 ± 5
G091.948+03.969	29	218 ± 20	5.3 ± 1.2	55 ± 17	4 ± 1e21	4 ± 1	29	24	150 ± 5
G091.808+04.142	30	118 ± 31	2.9 ± 1.3	43 ± 17	3 ± 1e21	3 ± 1	35	18	69 ± 5
G091.698+04.294	31	264 ± 30	6.5 ± 2.1	52 ± 17	4 ± 1e21	4 ± 1	41	26	153 ± 5
G091.783+04.197	32	88 ± 26	2.2 ± 1.0	41 ± 17	3 ± 1e21	3 ± 1	20	18	. . .
G091.855+04.119	33	856 ± 39	20.9 ± 3.2	163 ± 17	1 ± 1e22	11 ± 1	43	19	149 ± 5
G091.608+04.402	34	174 ± 23	4.2 ± 1.3	44 ± 17	3 ± 1e21	3 ± 1	32	18	4 ± 5
G092.177+03.762	36	375 ± 29	9.2 ± 2.3	57 ± 17	4 ± 1e21	4 ± 1	42	33	125 ± 5
G091.638+04.398	37	485 ± 21	11.8 ± 1.8	112 ± 17	7 ± 1e21	8 ± 1	26	22	115 ± 5
G091.813+04.201	38	127 ± 23	3.1 ± 1.0	49 ± 17	3 ± 1e21	3 ± 1	21	18	. . .
G091.861+04.172	39	756 ± 40	18.4 ± 3.5	123 ± 17	8 ± 1e21	9 ± 1	46	23	179 ± 5
G092.088+03.910	40	401 ± 33	9.8 ± 2.1	91 ± 17	6 ± 1e21	6 ± 1	34	21	84 ± 5
G092.168+03.821	41	214 ± 32	5.2 ± 1.7	58 ± 17	4 ± 1e21	4 ± 1	33	23	30 ± 5
G092.271+03.722	42	178 ± 39	4.3 ± 1.8	54 ± 17	4 ± 1e21	4 ± 1	31	18	166 ± 5
G092.125+03.893	43	713 ± 32	17.4 ± 3.0	94 ± 17	6 ± 1e21	7 ± 1	66	24	59 ± 5
G091.742+04.338	44	1021 ± 37	25.0 ± 3.7	111 ± 17	7 ± 1e21	8 ± 1	58	29	46 ± 5
G091.828+04.273	45	399 ± 23	9.8 ± 1.8	75 ± 17	5 ± 1e21	5 ± 1	29	24	144 ± 5
G092.197+03.853	46	160 ± 32	3.9 ± 1.4	54 ± 17	4 ± 1e21	4 ± 1	24	19	98 ± 5
G091.741+04.377	47	965 ± 35	23.6 ± 3.2	162 ± 17	1 ± 1e22	11 ± 1	47	21	164 ± 5
G092.269+03.787	48	2230 ± 32	54.5 ± 4.6	400 ± 17	3 ± 1e22	28 ± 1	30	29	154 ± 5
G091.872+04.277	49	111 ± 22	2.7 ± 1.0	44 ± 17	3 ± 1e21	3 ± 1	24	18	. . .
G091.935+04.188	50	62 ± 21	1.5 ± 0.7	28 ± 17	2 ± 1e21	2 ± 1	. . .	18	. . .
G091.838+04.341	51	360 ± 26	8.8 ± 2.0	54 ± 17	4 ± 1e21	4 ± 1	62	18	130 ± 5
G092.250+03.869	52	170 ± 29	4.2 ± 1.4	63 ± 17	4 ± 1e21	4 ± 1	27	22	. . .
G092.263+03.882	53	265 ± 26	6.5 ± 1.5	70 ± 17	5 ± 1e21	5 ± 1	32	18	13 ± 5
G091.926+04.343	54	138 ± 23	3.4 ± 1.0	45 ± 17	3 ± 1e21	3 ± 1	28	18	82 ± 5
G091.957+04.543	55	136 ± 18	3.3 ± 1.0	32 ± 17	2 ± 1e21	2 ± 1	49	18	104 ± 5

Notes.

[a] Identification number in Figure 3.

[b] Integrated flux of dust clump. The uncertainties are those produced by the *Bolocat* software package and are explained in detail in Rosolowsky et al. (2010).

[c] Estimated dust/gas clump mass for $T_D = 10$ K. Divide by 2.9 (1.9) for $T_D = 20$ K (15 K). The uncertainties are calculated from those on the integrated flux values.

[d] Peak flux in dust clump. The uncertainties are the rms noise in blank regions of sky.

[e] Maximum H_2 column density estimated from peak flux. The uncertainties are calculated from the uncertainties on the peak flux values.

[f] Maximum visual extinction estimated from peak flux. The uncertainties are calculated from the uncertainties on the peak flux values.

[g] $1/e$ major axis width of best-fit Gaussian in arcseconds. Errors are estimated to be at the 10% level.

[h] $1/e$ minor axis width of best-fit Gaussian in arcseconds. The fitting process is constrained to produce a minor axis greater than 18″.4, i.e., the $1/e$ width of the Bolocam beam at 1.1 mm. In the table, therefore, a value of 18″ indicates that the fitting process did not resolve the clump. Errors are estimated to be at the 10% level.

[i] Position angle of best-fit Gaussian in degrees east of north. The uncertainties are estimated from the 10% errors on the Gaussian fit major and minor axis values.

was likely severely incomplete. The slope of $\alpha = 1.5$ from 0.6 to 5 $M_\odot$ was found to be similar to the Salpeter initial stellar mass function (IMF) which has $\alpha = 1.35$ (Salpeter 1955). Our best-fit power law (from 2 to 20 $M_\odot$) has a slope of $\alpha = 1.2 \pm 0.15$ and is seen overlaid on the observed mass function in Figure 11. For comparison, both $\alpha = 0.5$ and 1.5 are also shown. The mass function in our survey region therefore seems very similar to that observed in ρ Oph by Johnstone et al. (2000) between similar masses. Enoch et al. (2006) noted that for the Perseus star-forming region, the power-law slopes were similar to those found by Johnstone et al. (2000) for ρ Oph, and also similar to those found by Chabrier (2003) for the local stellar IMF.

5. CONCLUSIONS

We have described a new 1.1 mm continuum emission map of the 1 deg^2 Braid Nebula star formation region in Cygnus OB7. In this map, we have detected 55 cold dust clumps with masses ranging from 1.5 to 54 $M_\odot$ (for $T_D = 10$ K). Our main conclusions are as follows.

1. Of the 55 dust clumps detected, 11 have associated *IRAS* sources. If we consider dust clumps with associated *IRAS* sources to be protostellar objects, then this fraction (i.e., 20%) differs significantly from the fraction of protostellar to starless clumps in the Taurus star formation region (i.e., 50%). However, if we consider the central $10' \times 10'$ region of the 1.1 mm map (centered on the Braid Star) then the fraction of protostellar to starless clumps is considerably higher (∼50%) and therefore similar to the fraction observed in the Taurus.
2. A large number of millimeter clumps (∼80%) do not exhibit far-IR emission. We classified these as starless in nature and possible sites of future star formation. We have not attempted to separate pre-stellar cores from starless clumps due to the complex and uncertain nature of the analysis.
3. Within the $40' \times 30'$ extent of the optical Hα image of the region shown in M10, ∼20% of the millimeter clumps are associated with optical stars. It is probably the case, however, that optical stars along the line of sight to the millimeter clumps confuse true physical associations.
4. Both FUor-like objects in the field (the Braid Star and HH 381 IRS) possess strong millimeter continuum emission. This suggests that these objects are relatively young in nature and that FUor-like eruptions occur at the very earliest stages of stellar pre-main-sequence evolution.
5. Of the sources studied in M03, A09, and M10, the optical monopolar nebula sources CN 1, 7, and 8, the optical bipolar jet source CN 2, and the young nebulous point-source CN 3 are not detected at millimeter wavelengths. This may imply for these objects that perhaps by the time a cavity (monopolar or bipolar) is created in the surrounding molecular cloud, the bulk of the cold circumstellar disk has been accreted onto the star.
6. The wide range of evolutionary states encountered in this region, i.e., from starless clumps to optically visible T Tauri stars, suggests that star formation is an ongoing process rather than a one-time occurrence.

We thank Alexander Laurich, Andrew Battisti, and Tucker Gilman for taking the observations presented above during UH TAC allocated observing time. We acknowledge the Caltech Submillimeter Observatory staff for their expert assistance during the acquisition of these data and in particular, Jack Sayer and Sunil Golwala for answers to the many questions posed on observing techniques and optimum data reduction techniques. We are indebted to Jonathan Williams for help in pre-observing preparation, Erik Rosolowsky for kindly providing GPS consistent post-data reduction analysis, and Melissa Enoch for valuable information on clump mass determination. We thank the University of Hawaii Time Allocation Committee for allocating the two nights during which these observations were made. The authors recognize and acknowledge the very significant cultural role and reverence that the summit of Mauna Kea has always had within the indigenous Hawaiian community. We are most fortunate to have the opportunity to conduct observations from this sacred mountain.

REFERENCES

Ambartsumian, V. A. 1971, Astrofizika, 7, 557
Andre, P., Ward-Thompson, D., & Barsony, M. 1993, ApJ, 406, 122
Aspin, C., et al. 2009, AJ, 137, 431 [A09]
Bergin, E. A., & Tafalla, M. 2007, ARA&A, 45, 339
Chabrier, G. 2003, PASP, 115, 763
Cohen, M. 1980, AJ, 85, 29
Davis, C. J., et al. 2010, MNRAS, 405, 759
Devine, D., Reipurth, B., & Bally, J. 1997, in IAU Symp. 182, Herbig-Haro Objects and the Birth of Low Mass Stars, ed. F. Malbet & A. Castets (Cambridge: Cambridge Univ. Press), 91
di Francesco, J., Evans, N. J., II, Caselli, P., Myers, P. C., Shirley, Y., Aikawa, Y., & Tafalla, M. 2007, in Protostars and Planets V, ed. B. Reipurth, D. Jewitt, & K. Keil (Tucson, AZ: Univ. Arizona Press), 17
de Zeeuw, P. T., Hoogerwerf, R., de Bruijne, J. H. J., Brown, A. G. A., & Blaauw, A. 1999, AJ, 117, 354
Enoch, M. L., et al. 2006, ApJ, 638, 293
Frerking, M. A., Langer, W. D., & Wilson, R. W. 1982, ApJ, 262, 590
Glenn, J., et al. 1998, Proc. SPIE, 3357, 326
Glenn, J., et al. 2009, in ASP Conf. Ser. 417, Submillimeter Astrophysics and Technology, ed. D. C. Lis, J. E. Vaillancourt, P. F. Goldsmith, T. A. Bell, N. Z. Scoville, & J. Zmuidzinas (San Francisco, CA: ASP), 277
Greene, T. P., Aspin, C., & Reipurth, B. 2008, AJ, 135, 1421
Herbig, G. H. 1989, Low Mass Star Formation and Pre-main Sequence Objects, ed. B. Reipurth (Garching: ESO), 233
Hiltner, W. A. 1956, ApJS, 2, 389
Johnstone, D., Wilson, C. D., Moriarty-Schieven, G., Joncas, G., Smith, G., Gregersen, E., & Fich, M. 2000, ApJ, 545, 327
Khavtassi, J. Sh. 1960, Atlas of Galactic Dark Nebulae (Tbilisi: Abastumani Observatory)
Laurent, G. T., et al. 2005, ApJ, 623, 742
Lee, C. W., & Myers, P. C. 1999, ApJS, 123, 233
Lynds, B. T. 1962, ApJS, 7, 1
Magakian, T. Y., et al. 2010, AJ, 139, 969 [M10]
Melikian, N. D., & Karapetian, A. A. 2001, Astrophysics, 44, 216
Melikian, N. D., & Karapetian, A. A. 2003, Astrophysics, 46, 282
Movsessian, T. A., Khanzadyan, T., Aspin, C., Magakian, T. Y., Beck, T., Moiseev, A., Smith, M. D., & Nikogossian, E. H. 2006, A&A, 455, 1001 [M06]
Movsessian, T., Khanzadyan, T., Magakian, T., Smith, M. D., & Nikogossian, E. 2003, A&A, 412, 147
Ossenkopf, V., & Henning, T. 1994, A&A, 291, 943
Reid, M. A., Wadsley, J., Petitclerc, N., & Sills, A. 2010, ApJ, 719, 561
Reipurth, B., & Aspin, C. 1997, AJ, 114, 2700
Reipurth, B., & Schneider, N. 2008, in Handbook of Star Forming Regions, ed. B. Reipurth (ASP Monograph, Vol. 4; San Francisco, CA: ASP), 36
Rosolowsky, E., et al. 2010, ApJS, 188, 123
Rowles, J., & Froebrich, D. 2009, MNRAS, 395, 1640
Salpeter, E. E. 1955, ApJ, 121, 161
Schmidt, K. H. 1958, Astron. Nachr., 284, 76
Ward-Thompson, D., André, P., Crutcher, R., Johnstone, D., Onishi, T., & Wilson, C. 2007, in Protostars and Planets V, ed. B. Reipurth, D. Jewitt, & K. Keil (Tucson, AZ: Univ. Arizona Press), 33